

Temperature-Dependent Hypersonic Flow Patterns of Expanding High-Density Metal Vapor Plasma from Capillary Source Simulating Plasma Flow Following a Fusion Disruption

Rudrodip Majumdar¹ · Mohamed Bourham¹

Published online: 14 October 2015
© Springer Science+Business Media New York 2015

Abstract Capillary discharge devices generating electrothermal plasmas from ablation of a liner material exposed to high heat flux are adequate devices to simulate fusion disruptions. Expansion of capillary-generated plasma into large volume simulates the evolution of the aerosol and plasma particulates into the reactor vacuum vessel. Effect of non-linearity and plasma bulk temperature on the adiabatic compressibility index was previously investigated showing considerable effect on the bulk flow parameters of polycarbonate plasma formed by the ablation of the capillary inner wall. In a fusion reactor, metals in the plasma-facing components such as the divertor, limiter, and first wall, will experience evaporation and formation of metal-vapor plasmas. Mathematical models have been developed to investigate the adiabatic compressibility index of ionized bulk metal vapors taking into account atomic and cluster ionization of metals, in addition to the effect of plasma bulk temperature and other nonlinearities. An important aspect of this current work is the distinction of the ionized states of metallic species instead of temperature-dependent lumped effective atomic number.

Keywords Electrothermal plasma expansion · Metal vapor plasma · Adiabatic compressibility index · Fusion disruption · PFC disruption · Particulate expansion

Introduction

Formation of metal-vapor plasmas in a pulsed capillary discharge generates high-density electrothermal plasma from the ablation of the metallic liner material with typical number densities in the range of 10^{26} – 10^{27} m⁻³, and temperatures in the range 1–5 eV [1]. The saturated vapor pressure and the dynamic temperature of molten metal largely affect the formation of the metal vapor plasma and its distribution. Purity and bulk density of the plasma is dependent on the liner material and device dimensions. Inappropriate arc conditions, lack of arc control, contamination on the electrode surfaces or electrode sever erosion may lead to metal vapor contamination [2–6]. Even the clusters coming out of the ablated metal surface may lead to formation of dusty plasma as it is quite commonly found in plasmas with an electron temperature below 10 eV. In such a case the plasma is not fully ionized, and thus the ions tend to collide with neutral atoms as well as the clusters. In the experiments under consideration, where the screening length is typically less than a millimeter, and the plasma pressure is in hundreds of MPa, collisionality could be quite significant and hence the cluster formation is becoming eminent.

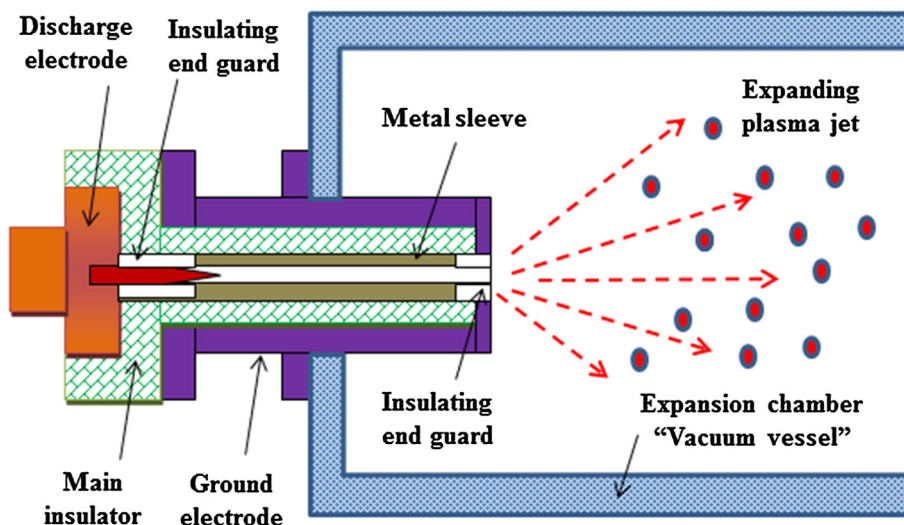
Unlike the case of insulating materials like Lexan or other non-conductive polycarbonate resins, a capillary discharge system with ablative metallic sleeve will have to be equipped with insulating ends to prevent short circuiting. A 1.0 cm long insulating guard in tubular shape is kept at each side of the metallic sleeve, which keeps the metallic sleeve floating and prevents short-circuiting the discharge current. The capillary in this configuration, as illustrated in Fig. 1, is connected to an expansion volume to simulate the flow into a fusion reactor vacuum vessel following a disruption event. The capillary source and the expansion

✉ Rudrodip Majumdar
rmajumd@ncsu.edu

Mohamed Bourham
bourham@ncsu.edu

¹ Department of Nuclear Engineering, North Carolina State University, Raleigh, NC 27695, USA

Fig. 1 Schematic diagram of a capillary discharge with ablative metallic sleeve connected to an expansion chamber simulating the fusion vacuum vessel



chamber simulate the divertor and the vacuum vessel, respectively.

To investigate the compressibility index in metal vapor plasma, in the simulation of fusion disruption, six metals were chosen as sleeve materials for their possible application in various plasma facing components; namely tungsten (W), molybdenum (Mo), iron (Fe), Chromium (Cr), Titanium (Ti) and aluminium (Al). The ETFLOW solver [7] has been run for multiple values of peak discharge current covering a range of 40–100 kA, for all selected metal liners. The ETFLOW calculates the temperature T (eV), pressure P (MPa), number density N_p (particles/m³), bulk density ρ (kg/m³), plasma bulk velocity V_{bulk} (m/s) and the total ablated metal mass M_{abl} (mg) at each axial node. The peak values at the last node, the capillary exit, are taken as the values of interest in simulating the plasma flow and expansion into the vacuum vessel. Ionization of individual atoms, as well as the cluster formation and subsequent ionization in the ablated metal-vapor plasma bulk, have been taken into account. In the present case, the first and the second ionization have been considered for isolated atoms, as well as the smallest atomic cluster (as a dimer having a single positive charge). The effect of plasma bulk temperature and the effective atomic numbers on the metal-vapor plasma bulk flow parameters have been investigated. As well known in the compressible flow regime, the adiabatic compressibility index (γ_p) is an important aspect that significantly affects the supersonic flow patterns. In this work mathematical models for the adiabatic compressibility index of partially ionized metal vapor have been proposed, that include plasma bulk temperature, atomic ionization energies and corresponding effective atomic numbers, dimer ionization energy and some predictive parameters that account for associated non-linearity as well as non-ideality.

Temperature-Dependent Compressibility Index Models

The isolated atoms or the monomers and the dimers being considered as the main constituents of the partially ionized high density metal vapor bulk; assuming the non-interacting, ideal gas behaviour of the constituents in a mixture of monoatomic and diatomic gases, one would prefer a linear approximation approach in finding the adiabatic compressibility index of the system resulting in an approximate value of $\gamma_p \approx (\gamma_{\text{Mono}} + \gamma_{\text{dia}})/2 \approx 1.53$. But partially ionized, very high density, high temperature, high pressure electrothermal plasmas exhibit highly non-linear behavior and the modeling of adiabatic compressibility index as a function of plasma bulk temperature becomes much more complicated. Two similar, yet different models for the adiabatic compressibility index (γ_p) have been proposed in this work. For each model four cases have been presented, which essentially make the formulae quite versatile and capable of explaining any irregular changes that might occur in the parameter profiles under different experimental conditions. The first model for γ_p is given below in Eq. (1).

$$\left. \begin{aligned} \frac{\gamma_p}{\gamma_p - 1.53} &= 1.1 + 0.25 * \frac{\left\{ a_1 \left(\frac{E_{I1}}{T_p} \right)^{a_2} + b_1 \left(\frac{E_{I2}}{T_p} \right)^{b_2} + c_1 \left(\frac{E_{Dim}}{T_p} \right)^{c_2} \right\}}{(1 + Z_{\text{comb}}^*)^d}, \\ (0.25 \leq T_p (\text{eV}) \leq 10) & \\ \text{where, } Z_{\text{comb}}^* &= (Z_1^{k_1} + Z_2^{k_2})^{\frac{1}{k_1 + k_2}} \\ \gamma_p (T_p < 0.25 \text{ eV}, Z_{\text{comb}}^*) &= \gamma_p (T_p = 0.25 \text{ eV}, Z_{\text{comb}}^*) \\ \gamma_p (T_p > 10 \text{ eV}, Z_{\text{comb}}^*) &= \gamma_p (T_p = 10 \text{ eV}, Z_{\text{comb}}^*) \end{aligned} \right\} \quad (1)$$

Here E_{I1} and E_{I2} are the ionization energies corresponding to the first and second ionizations respectively,

for an isolated atom in the gaseous phase. E_{Dim} is dimer ionization energy, T_p is the plasma bulk temperature in eV, Z_1 and Z_2 are the effective atomic numbers in the first and second ionization of isolated atom, respectively. The parameters $a_1, a_2, b_1, b_2, c_1, c_2, k_1, k_2$ and d are chosen intuitively and they take into account non-ideal as well as non-linear effects associated with the system. Four specific cases defined by four sets of values of the above mentioned parameters were investigated. These cases will enable an insight into the effect of dynamically changing γ_p on the metal vapor plasma flow characteristics. Table 1 lists the selected values of the parameters for each case.

For all selected metals, the plots for $\gamma(T_p)$ will follow a similar profile. The departure from one case to another will also be very similar, as a generic mathematical model has been used. The values of $\gamma(T_p)$ as a function of T_p for tungsten using Model 1 are illustrated in Fig. 2. The adiabatic compressibility index increases with the increase in the plasma temperature for all cases with less increase for case 1, which appears to be more flat. Strong increase is obvious for cases 3 and 4, almost a factor of 2 higher at the highest temperature (10 eV) as compared to the lowest temperature of 0.25 eV.

Model 2 is somewhat similar to Model 1, with a major difference in writing the parameter d as the exponent to a mathematical expression that contains the combined optimized orbital exponent Z_{comb}^* (as defined in Eq. 1), which includes the individual optimized orbital exponents Z_1 and Z_2 , respectively. Essentially this means for higher values of d , the value of γ_p will depend on a polynomial of Z_{comb}^* manifesting a higher extent of non-linearity. The effective nuclear charge increases with the increase in the cluster size [8]. Thus, by tuning the non-linearity parameters in the expression of adiabatic compressibility index to suitable values, such that Z_{comb}^* covers an adequately varied range of numerical values; the effect of the cluster formation and subsequent ionization on the bulk plasma flow characteristics can be computed. In case of Model 2, single

power on each of the individual optimized orbital exponents has been used. Model 2 is given mathematically in Eq. (2):

$$\left. \begin{aligned} \frac{\gamma_p}{\gamma_p - 1.53} &= 1.2 + 0.15 * \frac{\left\{ a'_1 \left(\frac{E_{I1}}{T_p} \right)^{a'_2} + b'_1 \left(\frac{E_{I2}}{T_p} \right)^{b'_2} + c'_1 \left(\frac{E_{Dim}}{T_p} \right)^{c'_2} \right\}}{\left(r'_1 Z_1^{s'_1} + r'_2 Z_2^{s'_2} \right)}; \\ (0.25 \leq T_p(eV) \leq 10) \\ \gamma_p(T_p < 0.25 eV, Z_1, Z_2) &= \gamma_p(T_p = 0.25 eV, Z_1, Z_2) \\ \gamma_p(T_p > 10 eV, Z_1, Z_2) &= \gamma_p(T_p = 10 eV, Z_1, Z_2) \end{aligned} \right\} \quad (2)$$

where, $E_{I1}, E_{I2}, E_{Dim}, T_p, Z_1$ and Z_2 bear the same meaning as in Model 1. $a'_1, a'_2, b'_1, b'_2, c'_1, c'_2, r'_1, r'_2, s'_1$ and s'_2 are the parameters that incorporates non-linearity and non-ideal effects. By using these models for γ_p , unexpected bulk irregularities and sudden variation in bulk flow characteristics can be explained, which may arise in various experimental scenarios. Table 2 lists the selected values of the parameters for each case.

The values of $\gamma(T_p)$ as a function of T_p for tungsten using Model 2 are illustrated in Fig. 3. Again, the adiabatic compressibility index increases with the increase in the plasma temperature for all cases as was previously shown when using Model 1. However, the rate of increase is not as high as that of Model 1.

The ionization energies for the single isolated metal atoms as well as the dimers have been taken from available well-known literature [9–12]. Some of the thermodynamic properties for specific metals were obtained from the published work of Desai [13]. The effective atomic numbers or the optimized orbital exponents were obtained using information available in published literature [14, 15]. Table 3 lists the ionization energies and the optimized orbital exponents of the selected metals. By incorporating these models for γ into the temperature sensitive supersonic flow equations as well as the shock models, as described in one of our previous work [18], it was shown that variation in bulk flow parameters of the metal vapor plasma is caused by non-linear changes in adiabatic compressibility index under isentropic conditions of the expanding plasma bulk.

Result and Discussion

Capillary exit parameters of interest have been tabulated in Tables 4, 5, 6 and 7 for four different peak discharge current values of 40, 50, 60 and 80 kA, respectively, which covers a reasonably wide range. The exit parameters were calculated using the 1-D ETFLOW code [7]. The exit parameters in Tables 4, 5, 6 and 7 are the plasma temperature T (eV), pressure P (MPa), number density N_p (#

Table 1 Non-linearity parameters for Model 1

Non-linearity parameter	Case 1	Case 2	Case 3	Case 4
a_1	1.00	1.00	1.00	1.00
a_2	0.04	0.08	0.27	0.38
b_1	1.00	1.00	1.00	1.00
b_2	0.04	0.08	0.27	0.38
c_1	1.00	1.00	1.00	1.00
c_2	0.04	0.08	0.27	0.38
k_1	0.90	0.20	0.70	0.80
k_2	0.90	0.20	0.70	0.80
d	0.85	0.40	0.80	0.60

Fig. 2 $\gamma(T_p)$ as a function of plasma temperature T_p for tungsten using Model 1

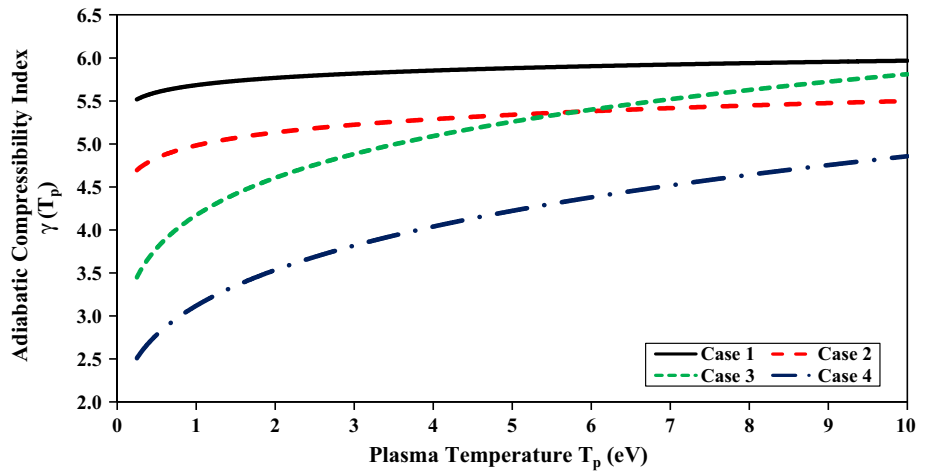


Table 2 Non-linearity parameters for Model 2

Non-linearity parameter	Case 1	Case 2	Case 3	Case 4
a'_1	1.00	1.00	1.00	1.00
a'_2	0.15	0.16	0.17	0.30
b'_1	1.00	1.00	1.00	1.00
b'_2	0.15	0.16	0.17	0.30
c'_1	1.00	1.00	1.00	1.00
c'_2	0.15	0.16	0.17	0.30
r'_1	0.70	0.70	0.70	0.20
r'_2	0.30	0.30	0.30	0.20
s'_1	0.45	0.75	1.05	0.60
s'_2	0.45	0.75	1.05	0.80

Table 3 Ionization energies and optimized orbital exponents

Metal	E_{I1} (eV)	E_{I2} (eV)	E_{Dim} (eV)	Z_1	Z_2
W	7.8640	16.10	14.43	3.550	3.550
Mo	7.0924	16.16	8.00	6.106	11.392
Fe	7.9024	16.19	6.10	5.434	5.434
Cr	6.7665	16.49	6.40	5.133	9.757
Ti	6.8281	13.57	6.13	4.817	4.817
Al	5.9858	18.83	6.21	4.117	4.066

m^3), density ρ (kg/m³), plasma exit velocity V_{bulk} (m/s) and total ablated mass M_{abl} (mg). Tables 4, 5, 6 and 7 clearly show that the peak magnitude of all plasma exit parameters increases with the increase of the peak discharge current.

However this increment in flow parameter is not linear with the increment in the peak discharge current. The capillary exit data obtained here are the bulk parameter values with which the metal vapor from ablation leaves the micro-nozzle and enters the converging section of the transition region [16–18].

Figures 4 and 5 display the Mach number profile along the axial direction into the transition region (Fig. 4) and the

Fig. 3 $\gamma(T_p)$ as a function of plasma temperature T_p for tungsten using Model 2

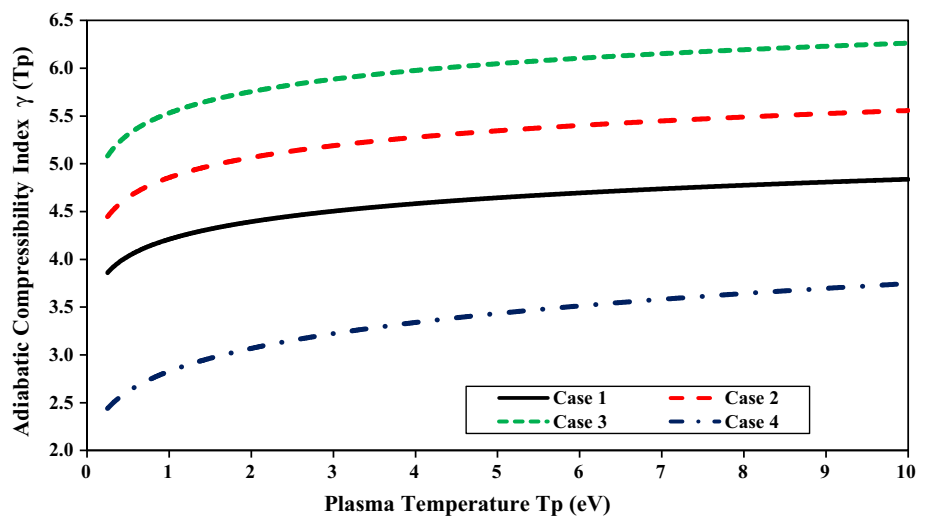


Table 4 Capillary exit parameters for peak discharge current $I = 40$ kA

Metal	T (eV)	P (MPa)	Np ($\#/m^3$)	ρ (kg/m^3)	V_{bulk} (m/s)	M_{abl} (mg)
W	2.780	395.192	1.12×10^{27}	341.857	1404.19	1039.37
Mo	2.680	412.061	1.03×10^{27}	164.057	1947.20	561.94
Fe	2.504	445.977	1.18×10^{27}	109.411	2424.76	411.83
Cr	2.503	451.773	1.09×10^{27}	94.097	2558.28	364.28
Ti	2.539	405.441	9.24×10^{26}	73.433	2797.41	290.83
Al	2.479	472.132	1.03×10^{27}	46.138	3529.53	189.50

Table 5 Capillary exit parameters for peak discharge current $I = 50$ kA

Metal	T (eV)	P (MPa)	Np ($\#/m^3$)	ρ (kg/m^3)	V_{bulk} (m/s)	M_{abl} (mg)
W	2.974	558.673	1.36×10^{27}	415.110	1480.69	1330.21
Mo	2.916	570.215	1.28×10^{27}	203.892	2022.15	716.24
Fe	2.646	588.561	1.43×10^{27}	132.587	2509.40	517.74
Cr	2.638	594.873	1.34×10^{27}	115.681	2667.26	458.67
Ti	2.691	591.277	1.17×10^{27}	92.982	2898.57	367.26
Al	2.640	632.541	1.25×10^{27}	55.997	3702.54	242.59

Table 6 Capillary exit parameters for peak discharge current $I = 60$ kA

Metal	T (eV)	P (MPa)	Np ($\#/m^3$)	ρ (kg/m^3)	V_{bulk} (m/s)	M_{abl} (mg)
W	3.188	705.855	1.62×10^{27}	494.475	1525.14	1621.51
Mo	3.088	726.104	1.52×10^{27}	242.124	2107.15	870.01
Fe	2.793	752.961	1.69×10^{27}	156.695	2601.42	624.15
Cr	2.782	768.145	1.59×10^{27}	137.265	2773.65	554.03
Ti	2.950	747.377	1.43×10^{27}	113.646	3147.54	446.31
Al	2.776	796.389	1.48×10^{27}	66.302	3804.79	294.29

Table 7 Capillary exit parameters for peak discharge current $I = 80$ kA

Metal	T (eV)	P (MPa)	Np ($\#/m^3$)	ρ (kg/m^3)	V_{bulk} (m/s)	M_{abl} (mg)
W	3.539	1114.000	2.18×10^{27}	665.409	1648.43	2201.05
Mo	3.408	1137.145	2.08×10^{27}	331.319	2259.81	1182.99
Fe	3.113	1130.056	2.26×10^{27}	209.547	2826.95	837.65
Cr	3.030	1166.647	2.14×10^{27}	187.742	2954.30	745.51
Ti	3.150	1335.867	1.98×10^{27}	157.358	3278.45	608.53
Al	3.024	1164.840	1.95×10^{27}	87.355	3995.50	398.23

expansion chamber (Fig. 5) showing that the Mach number is almost the same for all metals, which was previously discussed in our work on flow patterns and scaling of the flow bulk parameters [16, 17]. However, the minor deviations that arise are solely due to the changes in the adiabatic compressibility index, which has been modeled as a function of plasma bulk temperature as well as metal properties.

Figures 6, 7, 8, 9, 10, 11, 12 and 13 show the flow bulk parameters along the axial direction for $I_{peak} = 40$ kA for Case 1 (Model 1). Figure 6 shows the plasma temperature along the axial length in the transition region immediately after the ET source exit (0–0.007 m) for $I = 40$ kA, Case 1 (Model 1). The temperature drops

quickly inside this region for all tested metals. The temperature into the expansion chamber immediately after exiting the transition region and through the axial direction of the chamber is shown in Fig. 7, where the temperature rises and stays almost constant through the length of the chamber.

Figure 8 shows the plasma pressure along the axial length in the transition region immediately after the ET source exit (0–0.007 m) for $I = 40$ kA, Case 1 (Model 1). The pressure drops quickly inside this region for all tested metals, and has a similar profile of that of the temperature. The pressure into the expansion chamber immediately after exiting the transition region and through the axial direction of the chamber is shown in Fig. 9, where the pressure rises

Fig. 4 Mach number along the axial length in the transition region for $I = 40$ kA peak current for Case 1 (Model 1)

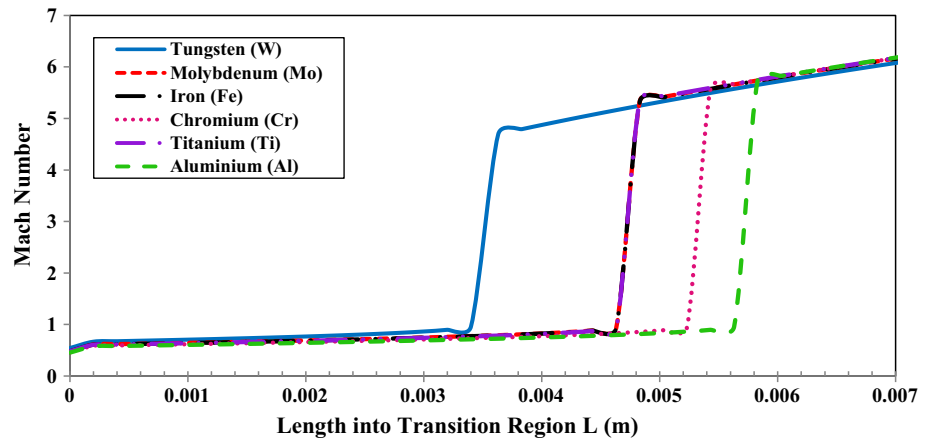


Fig. 5 Mach number along the axial length in the expansion chamber for Case 1 (Model 1)

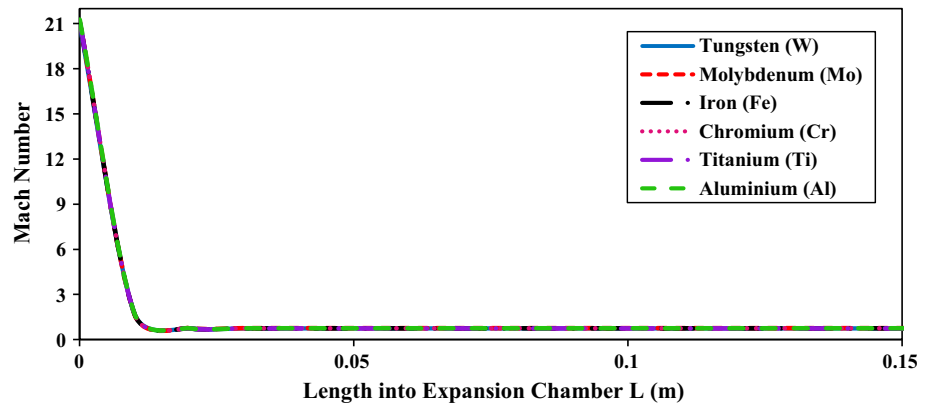
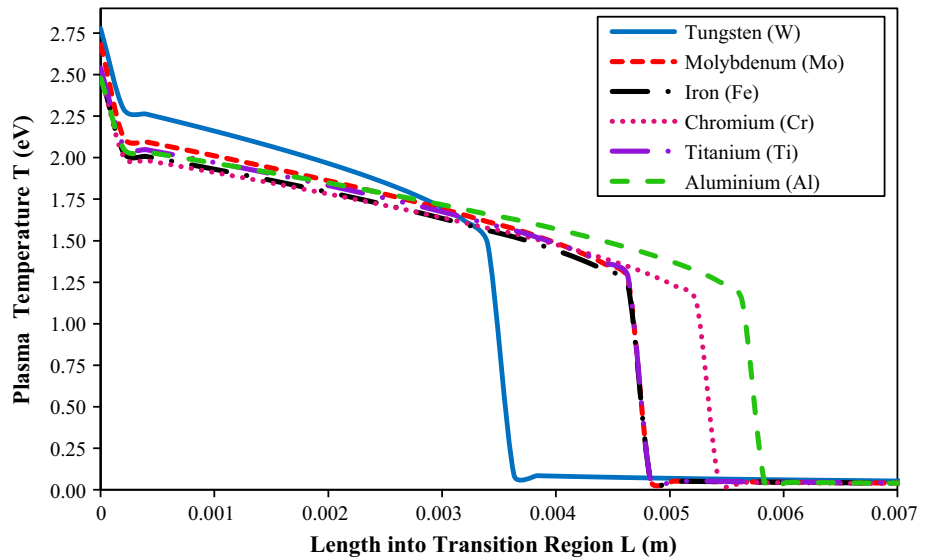


Fig. 6 Plasma temperature along the axial length in the transition region immediately after the ET source exit



and stays almost constant through the length of the chamber; a pattern similar to that of the temperature.

Figure 10 shows the plasma bulk velocity along the axial length in the transition region immediately after the ET source exit. The bulk velocity increases inside

this region for all tested metals and remains at a constant value after 0.007 m into the transition. The velocity into the expansion chamber immediately after exiting the transition region and through the axial direction of the chamber is shown in Fig. 11, where the

Fig. 7 Plasma temperature into the expansion chamber immediately after exiting the transition region and through the axial direction of the chamber

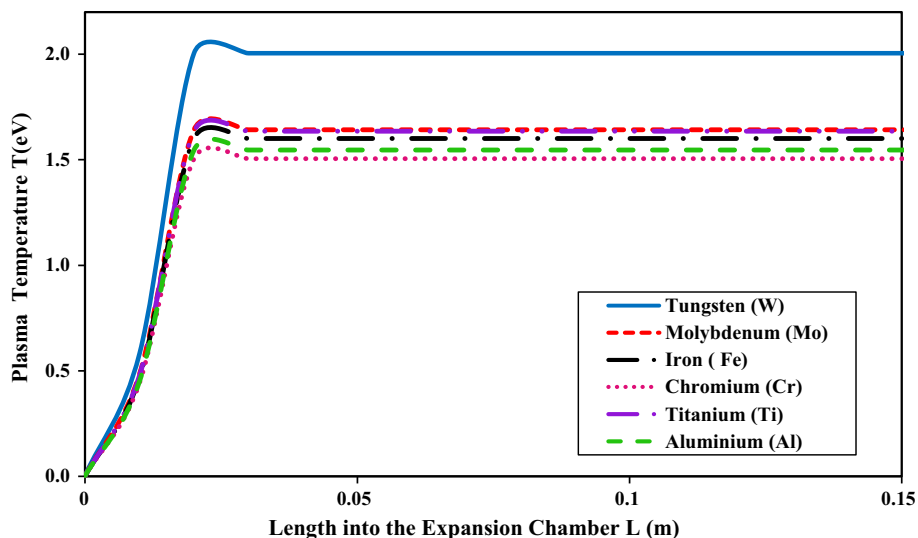


Fig. 8 Plasma pressure along the axial length in the transition region immediately after the ET source exit

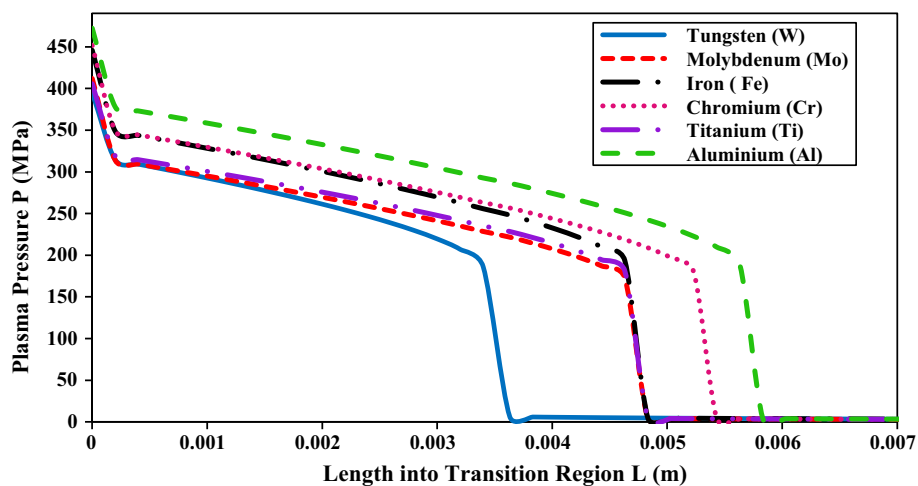


Fig. 9 Plasma pressure into the expansion chamber immediately after exiting the transition region and through the axial direction of the chamber

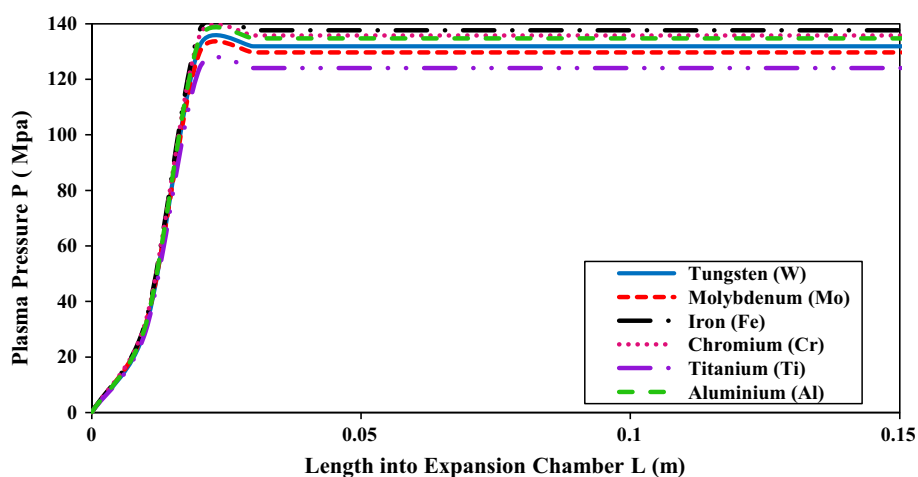


Fig. 10 Plasma bulk velocity along the axial length in the transition region immediately after the ET source exit

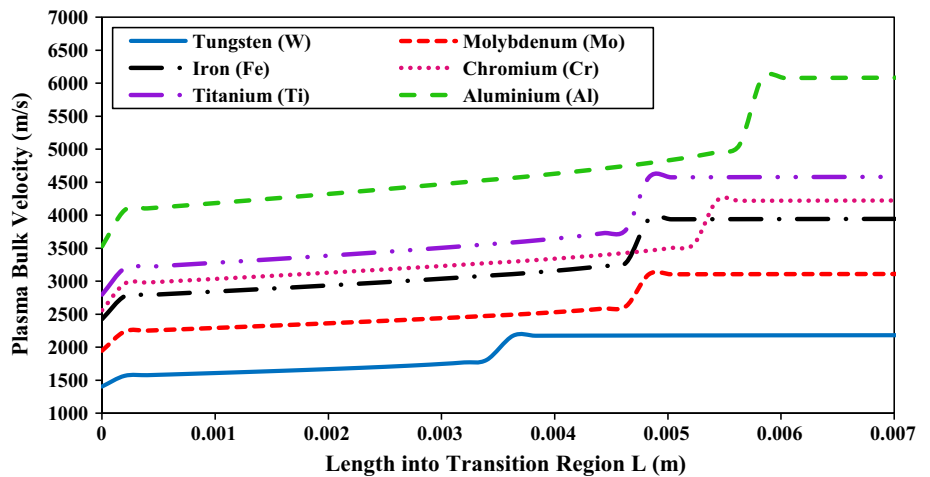


Fig. 11 Plasma bulk velocity into the expansion chamber immediately after exiting the transition region and through the axial direction of the chamber

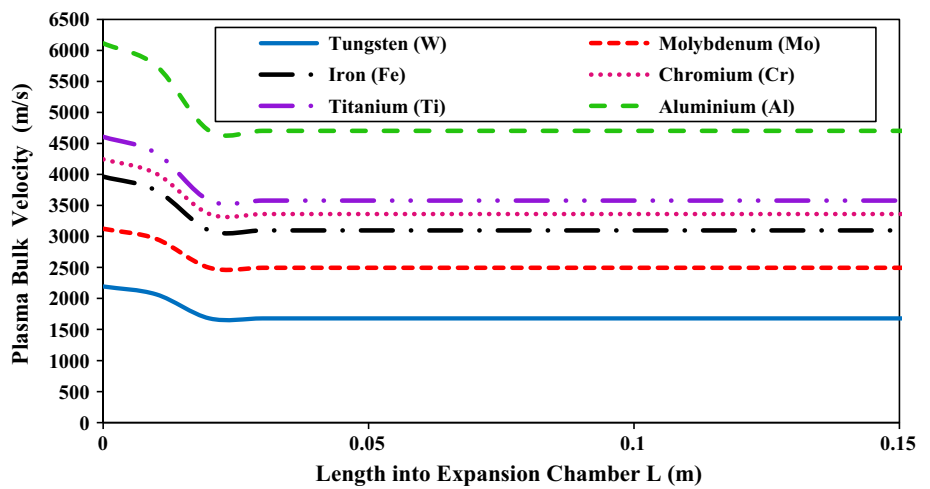
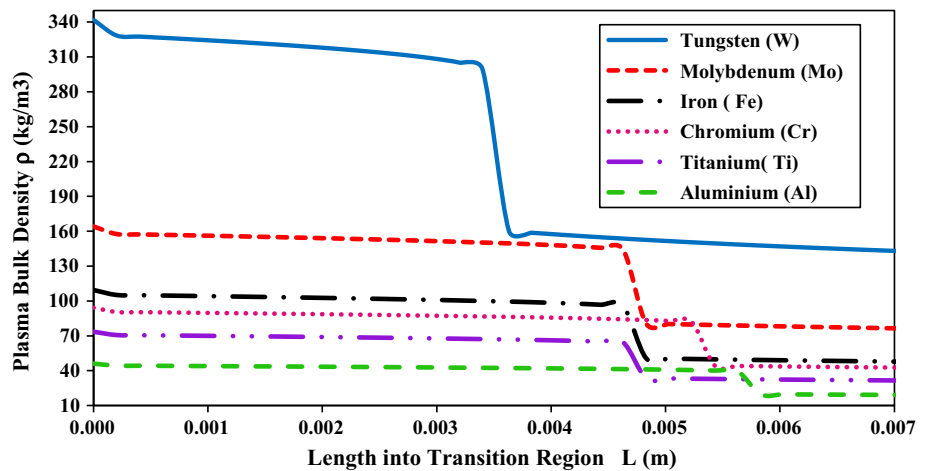


Fig. 12 Plasma bulk density along the axial length in the transition region immediately after the ET source exit

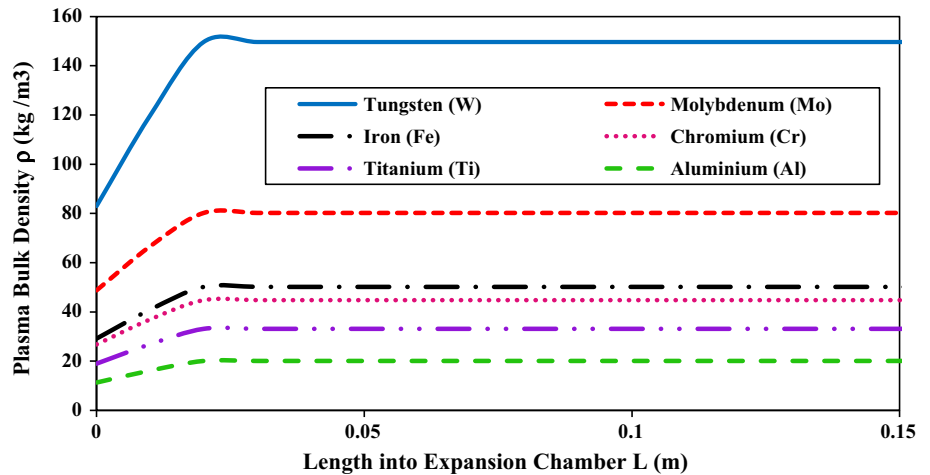


velocity slightly drops and stays almost constant through the length of the chamber.

Figure 12 shows the plasma bulk density along the axial length in the transition region immediately after the ET

source exit. The bulk density decreases inside this region for all tested metals and remains at a constant value after 0.007 m into the transition. Of interest is the higher drop rate in the density of tungsten as compared to all other

Fig. 13 Plasma bulk density into the expansion chamber immediately after exiting the transition region and through the axial direction of the chamber



tested metals. The density into the expansion chamber immediately after exiting the transition region and through the axial direction of the chamber is shown in Fig. 13, where the density increases and stays almost constant through the length of the chamber, with tungsten density rises higher than all other metals.

Table 8 shows that as the bulk plasma flow becomes sub-sonic inside the expansion chamber of uniform area cross-section, some of the steady-state flow parameters for the metal vapor plasmas differ in magnitude by quite a significant amount, whereas the other parameters do not vary that much. For example the steady state plasma bulk temperature for tungsten has been found to be 2.005 eV, which is the maximum value; whereas the lowest bulk temperature was found to be 1.505 eV in case of chromium vapor plasma. The steady-state plasma pressure is the maximum in case of iron ablated plasma and was found to be 137.67 MPa, while the minimum pressure has been estimated to be 124.05 MPa in the case where titanium sleeve was used. Looking at the above two flow parameters one does not see much difference between the maximum and the minimum steady-state values. But there is a significant change in case of the plasma bulk density. The

Table 8 Bulk flow parameter values at steady-state subsonic Condition inside the chamber

Metals	T (eV)	P (MPa)	ρ (kg/m ³)	V _{bulk} (m/s)
W	2.005	131.89	149.64	1678.86
Mo	1.642	129.70	80.21	2494.98
Fe	1.601	137.67	50.21	3095.51
Cr	1.505	135.82	44.77	3360.71
Ti	1.636	124.05	33.16	3576.98
Al	1.547	134.69	20.07	4704.17

maximum bulk density in the steady-state subsonic conditions has been estimated to be 149.64 kg/m³, for the tungsten vapor plasma, which is about 7 times larger than that found as the minimum of all others, a considerably low 20.07 kg/m³ for aluminium vapor plasma. For the plasma bulk velocity the trend is opposite. The maximum steady-state bulk speed of 4704.17 m/s occurs in case of aluminium vapor plasma and it is almost a factor of 3 higher than that of the minimum bulk velocity 1678.86 m/s in the case of tungsten.

In order to calculate the erosion thickness (Δx) of the metallic sleeves used in the simulation experiment to predict the extent of damage on the plasma facing surfaces prior to the supersonic expansion of the arc-ablated partially ionized aerosol mass, a new mathematical formula based on simple mass balance has been introduced:

$$M_{abl} = 2\pi \left(r_c + \frac{\Delta x}{2} \right) \Delta x L \rho_{Metal} \tag{3}$$

where, r_c is the inner radius of the capillary sleeve; Δx is the erosion thickness, L is the effective length of the capillary that is exposed to the radiant heat flux, ρ_{Metal} is the density of the metal used in the ablative sleeve and M_{abl} is the ablated mass as predicted by the ETFLOW plasma code [7]. Equation 3 leads to the following quadratic equation, which gives the erosion thickness for a particular metal exposed to radiant heat flux at a certain peak discharge current:

$$\frac{(\Delta x)^2}{2} + r_c \Delta x - \frac{M_{abl}}{(2\pi L \rho_{Metal})} = 0 \tag{4}$$

All the lengths are in meter, density is in kgm⁻³, ablated mass is in kg. The data presented in Tables 4, 5, 6 and 7 have been used in tandem with Eq. 4 to calculate the erosion thickness of the metals of interest for the listed

peak current values and are tabulated in Table 9 and plotted in Fig. 14.

As seen from Table 9, and Fig. 14, the ablated mass increases with the increase in the peak discharge current. The removal thickness is the largest in case of aluminium followed by titanium, chromium, iron, molybdenum and tungsten, respectively. Lesser removal thickness of a metal indicates a lesser extent of surface damage, which intuitively makes it a suitable candidate for being used as a plasma facing component under such high heat-flux conditions. The computational results obtained in this current work are in agreement with recent published experimental and computational research work on erosion of plasma-facing components that suggests tungsten and molybdenum to be good materials among the potentially durable metals which can be used in practical fusion reactors [19–22]. These results demonstrate the extent of disruption for each of the selected metals, which enables selection of the right metal for a particular plasma-facing component in future fusion reactors, as well as other applications in which metallic components are exposed to high heat flux deposition. As shown in Fig. 14, it appears that the erosion is close to linear increase with the increase in the magnitude of the peak discharge current.

Effect of Non-linearity on Tungsten Vapor Plasma: A Specific Case

The choice of a capillary running a peak discharge current of 60 kA is an attempt to run at higher current in order to look into non-ideal and non-linear behavior in the flow parameters associated with the adiabatic compressibility index. Tungsten is selected as a case study due to its importance as a potential plasma facing material in the divertor of fusion reactors. It is a material selected in recent research as the armor for the divertor upper vertical target, dome and cassette liner, as well as for lower baffle because of its unique resistance to ion and charge-exchange particle erosion in comparison with other materials [21]. Tungsten coated surfaces now represent a fraction of 65 % of all plasma facing components (~25 m²). The only two other major components that are not yet coated are the strike-point region of the lower divertor as well as the limiters at the low field side [21, 22].

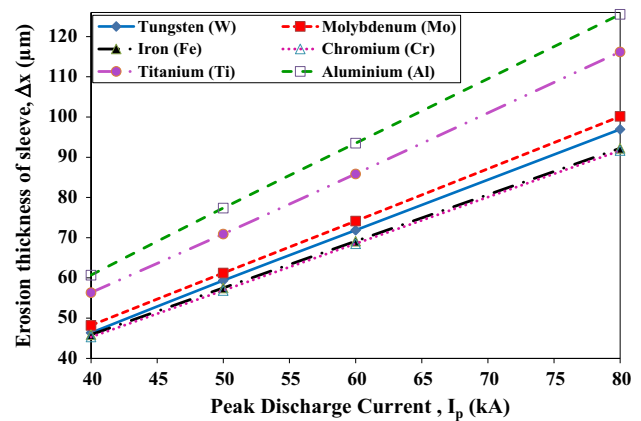


Fig. 14 Erosion thickness (μm) versus peak discharge current (kA)

Nonlinearity parameters from Tables 1 and 2, representing Models 1 and 2, respectively, are considered for this specific case of tungsten. Figure 15 shows the Mach number along the axial length for the peak current of 60 kA for Model 1, where it is obvious that the Mach number, being a very strong function of the cross-sectional area, hardly depends on the non-linearities associated with the adiabatic compressibility index and remains almost the same for all the cases, irrespective of the used γ model, typical to the behavior previously reported in Ref. [16–18].

The results of the tungsten case study will be illustrated for the axial length up to 0.3 meters. Figure 16 shows the plasma bulk density along the axial length for $I = 60$ kA using Model 1, where it is obvious that non-linearity and non-ideal effects can considerably affect the supersonic flow of the metal vapor bulk plasma. The plasma bulk density drops fast in the converging nozzle then rises in the converging section and reaches steady state in the expansion chamber. The same behavior is also typical when using Model 2 as illustrated in Fig. 17.

Similar behavior is also seen in the pressure profiles along the axial direction when using Model 1 (Fig. 18) and Model 2 (Fig. 19). The pressure drops fast in the transition section, rises at entry to the chamber and remains at a steady state through the expansion volume. However, this is not the case for the plasma bulk velocity as it increases in the transition section then drops to a steady state value into the expansion volume, as seen in Fig. 20 (Model 1) and Fig. 21 (Model 2).

Table 9 Erosion thicknesses of tested metals as a function of discharge current

I_{Peak} (kA)	$(\Delta x)_W$ μm	$(\Delta x)_{Mo}$ μm	$(\Delta x)_{Fe}$ μm	$(\Delta x)_{Cr}$ μm	$(\Delta x)_{Ti}$ μm	$(\Delta x)_{Al}$ μm
40	46.351	48.189	45.861	45.304	56.351	60.679
50	59.360	61.223	57.489	56.881	70.903	77.364
60	71.859	74.131	69.106	68.511	85.852	93.480
80	96.945	100.162	92.224	91.664	116.190	125.520

Fig. 15 Mach number along the axial length for a peak discharge current of 60 kA (Model 1)

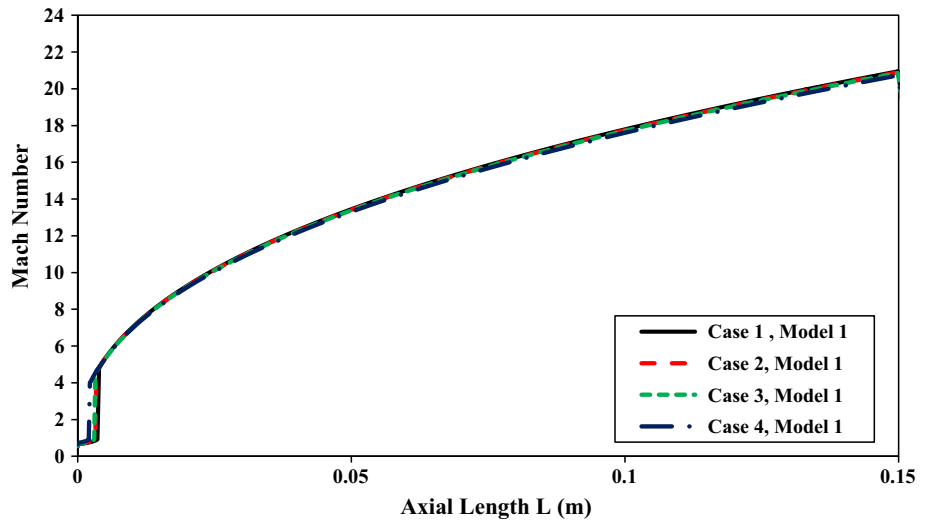


Fig. 16 Plasma bulk density along the axial length for I = 60 kA (Model 1)

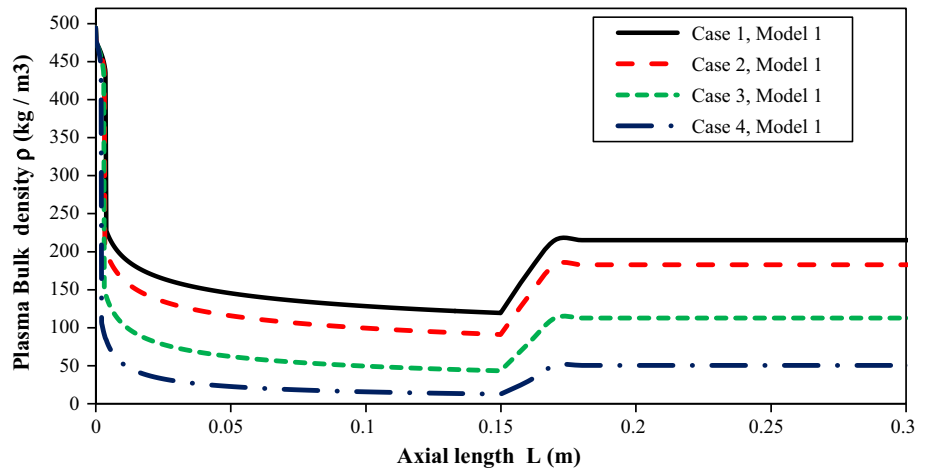


Fig. 17 Plasma bulk density along the axial length for I = 60 kA (Model 2)

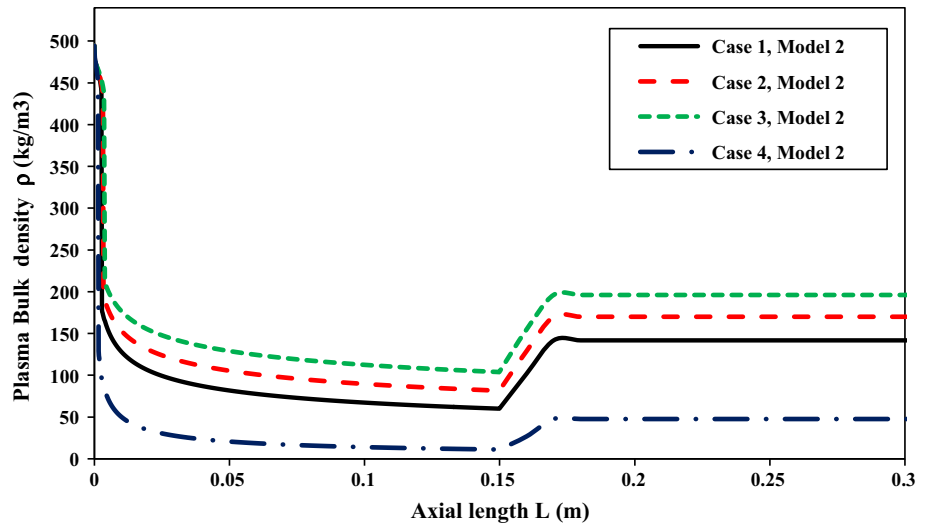


Fig. 18 Plasma pressure along the axial length for $I = 60$ kA (Model 1)

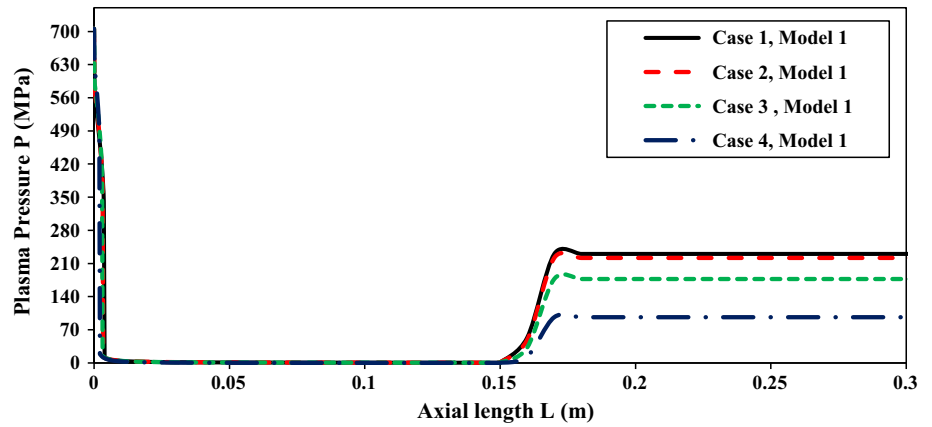
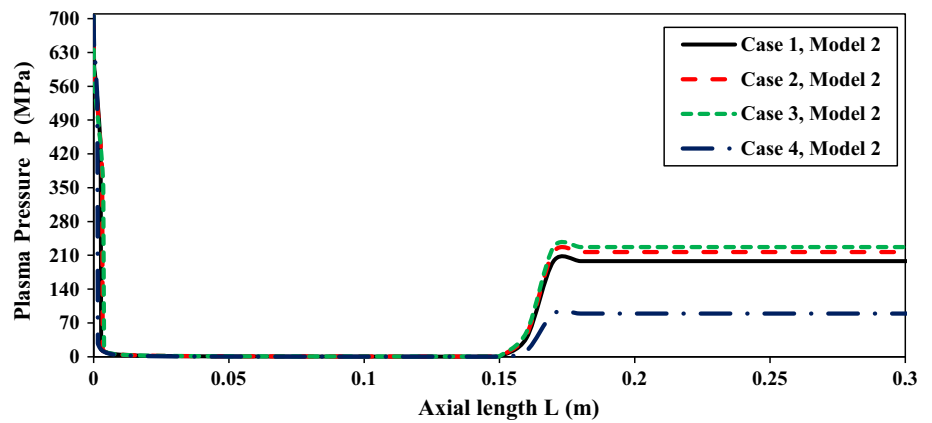


Fig. 19 Plasma pressure along the axial length for $I = 60$ kA (Model 2)



Plasma temperature, as seen in Fig. 22 (Model 1) and Fig. 23 (Model 2), follows the same behavior of density and pressure, it drops fast in the transition section, rises at entry to the chamber and remains at a steady state through the expansion volume. This behavior is expected due to the fact that the plasma kinetic pressure is dependent on both density and temperature. Tables 10 and 11 summarize the

results of the parameters for each of the four cases when using Model 1 (Table 10) and Model 2 (Table 11).

As has been seen in Figs. 16, 17, 18, 19, 20, 21, 22 and 23 it is obvious that non-linearity and non-ideal effects can affect the supersonic flow. All the bulk flow parameters exhibit significant changes, however plasma bulk temperature has been found to be least affected by the non-linear

Fig. 20 Plasma bulk velocity along the axial length for $I = 60$ kA (Model 1)

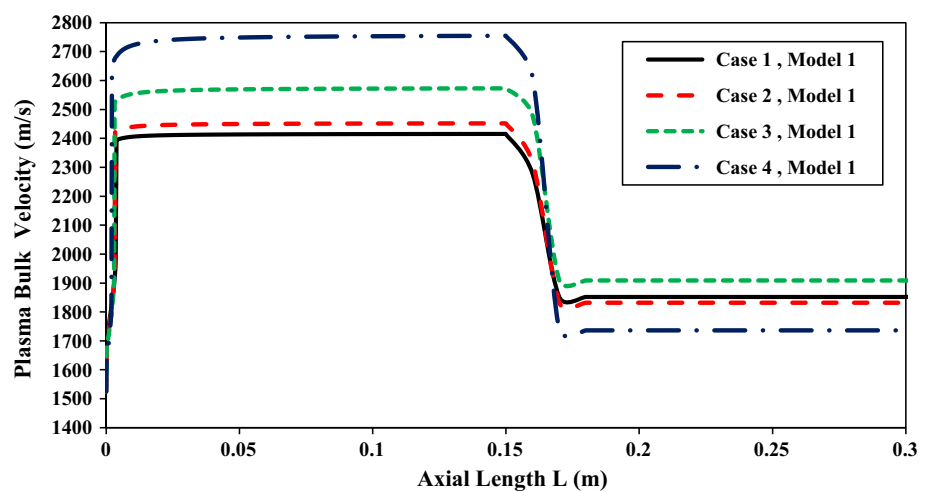


Fig. 21 Plasma pressure along the axial length for $I = 60$ kA (Model 2)

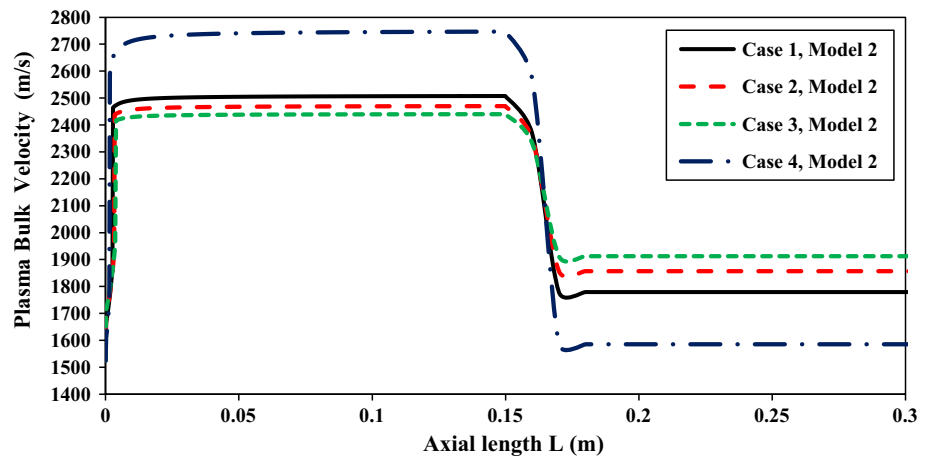


Fig. 22 Plasma temperature along the axial length for $I = 60$ kA (Model 1)

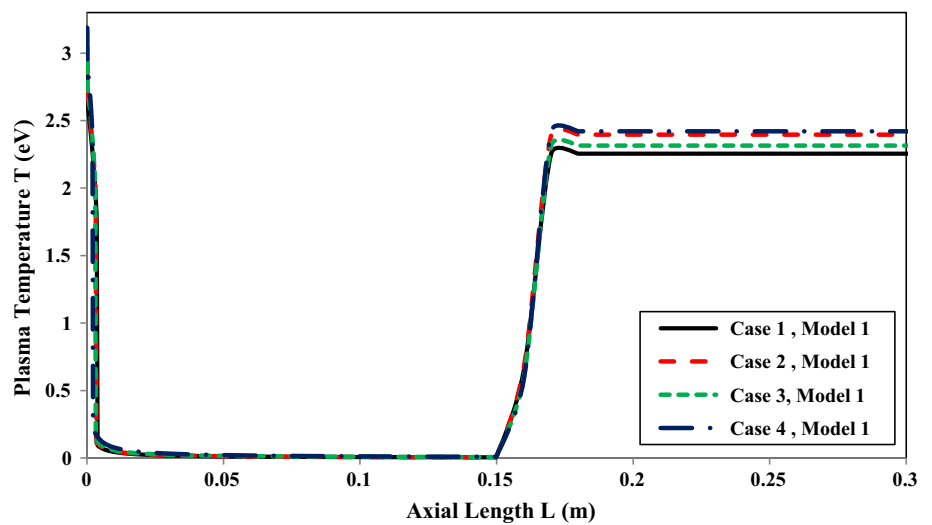
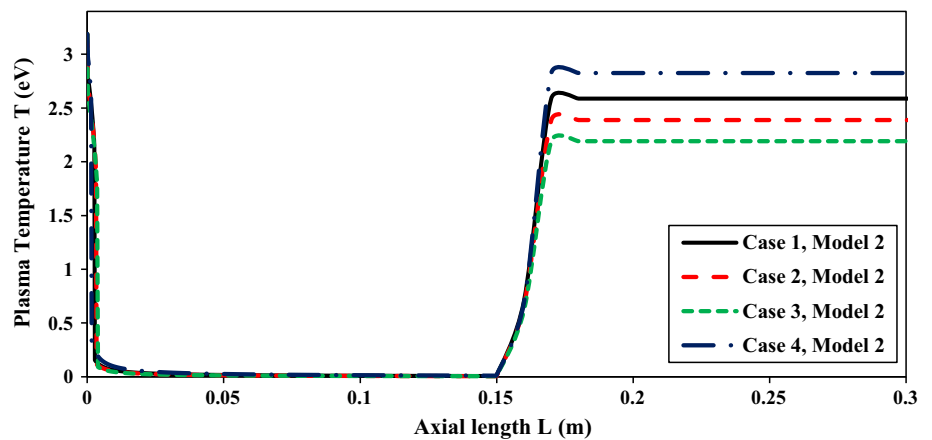


Fig. 23 Plasma temperature along the axial length for $I = 60$ kA (Model 2)



changes in the adiabatic compressibility index (γ) of the bulk plasma. In case of Model 1, extreme cases may see a swing in steady-state plasma bulk temperature by as much as 7.36 %, whereas in case of Model 2 this swing has been observed to increase up to 28.982 % with respect to the

lower end value, the actual differences being not too large. Plasma bulk density and plasma pressure have been observed to get affected by a large amount due to the non-linear effects. Steady-state plasma bulk density has been observed to differ by a significant amount; about a factor of

Table 10 Bulk flow parameter at steady-state subsonic condition inside the chamber for γ Model 1 using capillary exit data corresponding to $I_{\text{peak}} = 60$ kA

Steady-state flow parameters	Case 1	Case 2	Case 3	Case 4
T (eV)	2.25500	2.39600	2.31500	2.42100
P (MPa)	230.162	221.504	176.989	96.5570
ρ (kg/m ³)	215.211	182.764	112.669	50.4070
V_{bulk} (m/s)	1851.84	1832.11	1908.98	1736.65

Table 11 Bulk flow parameter at steady-state subsonic condition inside the chamber for γ Model 2 using capillary exit data corresponding to $I_{\text{peak}} = 60$ kA

Steady-state flow parameters	Case 1	Case 2	Case 3	Case 4
T (eV)	2.58800	2.38800	2.19100	2.8260
P (MPa)	197.988	216.557	226.909	89.345
ρ (kg/m ³)	141.786	170.105	196.082	47.779
V_{bulk} (m/s)	1779.27	1857.04	1912.67	1585.69

4.27 in case of Model 1, and by a factor of 4.10 in case of Model 2, the lowest bound being the reference point of the respective computational instances. Plasma pressure in the expansion chamber has been observed to differ by a factor of 2.38 in case of Model 1, and by a factor of 2.54 in case of Model 2, in each of the instances the lowest pressure being the reference point. Plasma bulk velocity, however exhibits a much lower sensitivity towards these non-ideal and non-linear effects. In case of Model 1, extreme case values differ by 9.92 % and the difference goes up to 20.62 % in case of Model 2. As the bulk velocity (V) is dictated by the sonic speed (a) at a certain temperature (T), pressure (P), and density (ρ); thus it depends also on the value of γ . The Mach number is $= V/a$, where $a = (\gamma P/\rho)^{1/2}$.

In the present set-up, the steady-state subsonic flow inside the expansion chamber is characterized by a constant Mach number ($Ma \approx 0.6\text{--}0.7$), irrespective of the various cases demonstrated in this work. Thus clearly it can be seen that for our purpose— $V \propto (\gamma P/\rho)^{1/2}$. From the models of adiabatic compressibility index, it can be seen that $(\gamma)^{1/2}$ does not differ much in the various cases of interest, even if the extreme limits are considered. Thus steady-state plasma velocity is dictated by the ratio of the plasma bulk pressure to the plasma bulk density. The higher the value (P/ρ), ratio the greater is the steady-state bulk velocity. Lower values of ρ in some cases indicate that there may be higher rate of recombination, cluster formation, or agglomeration in occasional instances resulting in an unexpected drop in the plasma bulk density, which results in a proportional decrease in the plasma pressure. These are the form of in-system physical hindrances which essentially slows down the steady state plasma flow. The minor changes in plasma bulk temperature indicate that the processes are energetically stable and consistent. Nevertheless, the non-linear effects help in determining the safety factor in designing the active volume as it should be able to hold the plasma with a sufficiently high bulk pressure.

Conclusion

In this work the effect of temperature-dependent adiabatic compressibility index on the supersonic plasma jet generated from arc-ablated metal sleeves has been investigated. Looking at the disruptive nature, one can decide upon proper metals for the plasma-facing components. Additionally added safety can also be ensured as nonlinearities have been taken into account to some extent. The observed deviation is attributed to the added parameters but helped to have an insight towards 1-D expansion behavior of moderate-temperate metal vapor plasmas.

References

1. J. Gilligan, M. Bourham, The use of an electrothermal plasma gun to simulate the extremely high heat flux conditions of a tokamak disruption. *J. Fusion Energ.* **12**(3), 311–316 (1993)
2. S.V. Kukhlevsky et al., Generation of pure, high-density metal-vapor plasma by capillary discharge. *Appl. Phys. Lett.* **74**(19), 2779–2781 (1999)
3. L.L. Raja, P.L. Varghese, Modeling of the electrothermal Ignitor metal vapor plasma for electrothermal-chemical guns. *IEEE Trans. Magn.* **33**(1), 316–321 (1997)
4. G.J. Dunn, S.D. Allemand, T.W. Eagar, Metal vapors in gas tungsten arcs: part I. spectroscopy and monochromatic photography. *Metall. Trans. A* **17A**, 1851–1863 (1986)
5. J. Kutzner, Metal vapor plasma jets in the high-current vacuum arcs, in *Proceedings of ISDEIV, XVIIth International Symposium on Discharges and Electrical Insulation in Vacuum*, Berkeley, CA, 1, July 21–26 1996, (1996), pp. 99–103
6. G.E. Dale, M.A. Bourham, Melt-layer erosion and resolidification of metallic plasma-facing components', in *Proceedings of 17th IEEE NPSS Symposium on Fusion Engineering*, vol. 2, San Diego, CA, 6–10 Oct 1997, (1997), pp. 892–895
7. L. Winfrey, J. Gilligan, A. Saveliev, M. Abd Al-Halim, M. Bourham, A study of plasma parameters in a capillary discharge with calculations using ideal and non-ideal plasma models for comparison with experiment. *IEEE Trans. Plasma Sci.* **40**(3), 843–852 (2012)

8. P. Sigmund, I.S. Bitensky, J. Jensen, Molecule and cluster bombardment: energy loss, trajectories and collision cascades. *Nucl. Instrum. Methods Phys. Res B* **112**(1–4), 1–11 (1996)
9. C.W. Bauschlicher, L.A. Barnes, P.R. Taylor, Lowest ionization potentials of Al_2 . *J. Phys. Chem.* **93**, 2932–2935 (1989)
10. A. Kalemios, A. Mavridis, The electronic structure of Ti_2 and Ti_2^+ . *J. Chem. Phys.* **135**, 134302 (2011)
11. A.E. Kramida, J. Reader, Ionization energies of tungsten ions: W^{2+} through W^{72+} . *At. Data Nucl. Data Tables* **92**, 457–479 (2006)
12. V.D. Lakhno, G.N. Chuev (eds.), *Physics of Clusters* (World Scientific Publishing, Singapore, 1998)
13. P.D. Desai, Thermodynamic properties of manganese and molybdenum. *J. Phys. Chem. Ref. Data* **16**(1), 91–108 (1987)
14. J.C. Slater, Atomic shielding constants. *Phys. Rev.* **36**, 57–64 (1930)
15. E. Clementi, D.L. Raimondi, W.P. Reinhardt, Atomic screening constants from SCF functions. II. atoms with 37 to 86 electrons. *J. Chem. Phys.* **47**(4), 1300–1307 (1967)
16. R. Majumdar, J.G. Gilligan, A.L. Winfrey, M.A. Bourham, Supersonic flow patterns from electrothermal plasma source for simulated ablation and aerosol expansion following a fusion disruption. *J. Fusion Energ.* **33**(1), 25–31 (2014)
17. R. Majumdar, J.G. Gilligan, A.L. Winfrey, M.A. Bourham, Scaling laws of bulk plasma parameters for a 1-D flow through a capillary with extended converging-diverging nozzle for simulated expansion into fusion reactor chamber. *J. Fusion Energ.* **34**(4), 905–910 (2015)
18. R. Majumdar, M.A. Bourham, Effect of plasma temperature and nonlinearity of the adiabatic compressibility index on flow parameters for hypersonic aerosol expansion following a plasma disruption. *J. Fusion Energ.* (2015). doi:[10.1007/s10894-015-9960-1](https://doi.org/10.1007/s10894-015-9960-1)
19. A. Hassanein, Prediction of material erosion and lifetime during major plasma instabilities in tokamak devices. *Fusion Eng. Des.* **60**, 527–546 (2002)
20. H. Bolt, V. Barabash, W. Krauss, J. Linke, R. Neu, S. Suzuki, N. Yoshida, ASDEX Upgrade Team, Materials for the plasma-facing components of fusion reactors, *J. Nucl. Mater.* **329**, 66–73 (2004)
21. R. Neu et al., Tungsten: an option for divertor and main chamber plasma facing components in future fusion devices. *Nucl. Fusion* **45**, 209–218 (2005)
22. J. Linke, High heat flux performance of plasma facing materials and components under service conditions in future fusion reactors. *Fusion Sci. Technol.* **57**(2T), 293–302 (2010)